The refined structure of human rhinovirus 16 at 2.15 Å resolution: implications for the viral life cycle

Andrea T Hadfield[1†], Wai-ming Lee[2], Rui Zhao[1‡], Marcos A Oliveira[1§], Iwona Minor[1], Roland R Rueckert[2] and Michael G Rossmann[1*]

Background: Rhinoviruses belong to the picornavirus family and are small, icosahedral, non-enveloped viruses containing one positive RNA strand. Human rhinovirus 16 (HRV16) belongs to the major receptor group of rhinoviruses, for which the cellular receptor is intercellular adhesion molecule-1 (ICAM-1). In many rhinoviruses, one of the viral coat proteins (VP1) contains a hydrophobic pocket which is occupied by a fatty acid-like molecule, or so-called 'pocket factor'. Antiviral agents have been shown to bind to the hydrophobic pocket in VP1, replacing the pocket factor. The presence of the antiviral compound blocks uncoating of the virus and in some cases inhibits receptor attachment. A refined, high-resolution structure would be expected to provide further information on the nature of the pocket factor and other features previously not clearly identified.

Results: The structure of native HRV16 has been refined to a resolution of 2.15 Å. The hydrophobic pocket in VP1 is observed in two alternative conformations. In one of these, the pocket is filled by a pocket factor and the protein structure is similar to virus–antiviral compound complexes. In the other conformation, the hydrophobic pocket is collapsed and empty. RNA bases stack against both a tryptophan and a phenylalanine residue on the internal surface of the viral capsid. Site-directed mutagenesis of the tryptophan, which is conserved across the picornaviruses, to nonconservative residues results in non-viable virus. Five symmetry-related N termini of coat protein VP4 form a ten-stranded, antiparallel β barrel around the base of the icosahedral fivefold axis. The N termini of VP1 are amphipathic α helices, which stack on the outside of this β barrel. The N termini of VP1 and VP4 have not been observed previously in rhinovirus structures.

Conclusions: The observation of a partially occupied hydrophobic pocket in HRV16 forms a missing link between HRV14, which is always observed with no pocket factor in the native form, and rhinovirus 1A and other picornaviruses (e.g. poliovirus, coxsackievirus) which contain pocket factors. The pocket factor molecules probably regulate viral entry, uncoating and assembly. Picornavirus assembly is known to proceed via pentamers, therefore, the interaction of RNA with the conserved tryptophan residues across twofold axes between pentamers may play a role in picornavirus assembly. The positioning of a cation on the icosahedral fivefold axes and the structure of the N termini of VP4 and VP1 around these axes suggest a mechanism for the uncoating of rhinoviruses.

Addresses: [1]Department of Biological Sciences, Purdue University, West Lafayette, IN 47907-1392, USA and [2]Bock Laboratories, Institute for Molecular Virology, University of Wisconsin, Madison, WI 53706, USA.

Present addresses: [†]Rosenstiel Center for Basic Medical Research, Brandeis University, Waltham, MA 0225, USA, [‡]Department of Chemistry and Biochemistry, University of Texas, Austin, TX 78712, USA and [§]Department of Microbiology and Immunology, University of North Carolina, Chapel Hill, NC 27599-7290, USA.

*Corresponding author.
E-mail: mgr@indiana.bio.purdue.edu

Key words: crystal structure, human rhinovirus 16, refinement, RNA, site-directed mutagenesis

Received: 4 December 1996
Revisions requested: 10 January 1997
Revisions received: 23 January 1997
Accepted: 24 January 1997

Electronic identifier: 0969-2126-005-00427

Structure 15 March 1997, 5:427–441

Introduction

Human rhinovirus 16 (HRV16), like other picornaviruses [1], is constructed from sixty copies of each of four viral proteins (VPs) arranged to form an icosahedral shell around a single strand of positive-sense RNA. The three major coat proteins, VP1, VP2 and VP3 (each with molecular weight of approximately 30 000), have the antiparallel β-barrel topology observed in many viral capsid proteins. The fourth, smaller protein, VP4 (molecular weight 7000), lies on the interior of the protein shell and is in contact with the packaged RNA. VP4 and VP2 are cleaved from a precursor, VP0, after the formation of protomers consisting of VP1, VP3 and VP0. This maturation cleavage is required for infectivity and happens after RNA packaging [2]. Assembly proceeds via pentamers, but it is not known whether RNA is packaged by accretion of pentamers or whether RNA is inserted into preformed empty particles.

The three-dimensional structure of HRV16 was previously determined at 3.5 Å resolution [3]. HRV16 and HRV14 [4] belong to the major receptor group of rhinoviruses [5], for which the cellular receptor is intercellular adhesion

molecule-1 (ICAM-1) [6,7]. There is a deep surface depression, the 'canyon', about each fivefold axis into which the ICAM-1 molecule has been shown to bind [8].

A number of antiviral compounds have been investigated crystallographically in complex with HRV14 [9], poliovirus 1 and poliovirus 3 [10], HRV1A [11], HRV16 [3] and coxsackievirus B3 [12]. The antiviral agents bind to the hydrophobic pocket in VP1 to block uncoating of the viral particles [13,14] and, in the case of the some rhinoviruses, also inhibit receptor attachment [15]. In the first studies of the antiviral compounds, it was suggested that the hydrophobic pocket may have significance in the viral life cycle [9]. This pocket binds a possibly cellular-derived 'pocket factor' [16] which may regulate capsid stability during cell entry [3,4].

Incubation of HRV14 with soluble receptor, reduction of pH and an increase in temperature to 52°C all induce structural changes in the virion that result in the loss of VP4 [3,4,17], externalization of VP1 [18] and production of non-infectious 'A' particles. RNA is subsequently lost from A particles in the formation of empty 80S particles. It has recently been shown that a possible intermediate in this reaction is a particle with partial loss of VP4 and no RNA, but which still has bound receptors [19]. VP4, released from the shell, may play a role in delivering the viral genome across the cell membrane. Release of VP4 from the virion is required for infectivity in HRV14 [2]. In poliovirus, the mature virion with a single mutation in VP4 is not infectious, although it is capable of normal uncoating to form 135S A particles lacking VP4 [20].

We report here the phase extension and refinement of the structure of HRV16 to 2.9 Å resolution, the diffraction limit of the original data set (data set I) [3]. In addition, new data with a minimum Bragg spacing of 2.15 Å (data set II) have been analyzed and used for an independent structural refinement. The biological significance of RNA stacking against a tryptophan residue was studied by introducing site-directed mutations at this position.

Results

Structure description of native HRV16

Refinement of the structure of HRV16 has allowed modeling of some features not observed in the 3.5 Å structure [3] (Table 1). Extra residues were modeled at the N and C termini of viral proteins 1, 2 and 4. The pocket factor noted in the original structure appears to be longer after refinement. The N-terminal myristate and RNA bases interacting with the viral protein coat have been identified on the interior surface of the viral shell. The refined structures of HRV16 determined from data sets I and II have significant differences only in the vicinity of the hydrophobic binding pocket in VP1, with a root mean square (rms) distance between corresponding Cα atoms in the two independently refined structures of 0.09 Å. The higher resolution data set II shows that residues 2088 and 3189 have two conformations, with approximately half occupancy of each (Note residue numbers are given in the form XNNN, where X represents the protein chain and NNN represents the sequence number of the residue within that chain). In the following descriptions, the structure derived from data set II will be discussed unless otherwise noted. The standard deviation of the electron density, σ, is taken as the variation between the electron densities of the 30 noncrystallographic asymmetric units in the averaging procedure. The relationship between this value and the 'average electron density', ρ_{av}, is approximately $2\sigma = \rho_{av}$.

Table 1

Structural observations for HRV16.

	Model	
	Oliveira *et al.* [3]	Present model
VP1	1005–1284	1001–1285 (complete VP1) (alternative conformations 1210–1218 using data set II)
VP2	2011–2259	2010–2261 (nine missing)
VP3	3001–3238	3001–3238 (complete)
VP4	4026–4044	4001–4007 4023–4044 (40 missing)
Pocket factor	8 carbon chain	12 carbon chain (partial occupancy using data set II)
Ion site	Identified as Ca^{2+}	Possibly Zn^{2+}
RNA	Not identified	Stacking against Tyr1055 and Trp2038
Myristate	Not identified	Head group modeled

VP1

The N terminus of VP1 forms an amphipathic helix

Every residue in VP1 could be seen clearly with main-chain density of at least 3.0 standard deviations, 3σ. The amphipathic helix, previously observed and modeled from residue 1005 to 1012 [3], is now seen to extend from 1001 to 1012. The sidechains for residues 1001–1004 are not visible in the averaged electron-density map. This amphipathic helix lies on the interior of the virus particle along the icosahedral fivefold axis.

Hydrophobic binding pocket

The hydrophobic pocket is 'open' and contains a pocket factor in the structure derived from data set I, as observed by Oliveira *et al.* [3]. This open conformation is similar to that observed in other rhinoviruses and enteroviruses that contain a pocket factor or an antiviral compound. The pocket factor is more clearly defined after refinement, and its size and shape are consistent with a twelve-carbon fatty acid ($C_{12}O_2H_{22}$). The head group of the modeled fatty acid lies at the more solvent accessible end of the

Figure 1

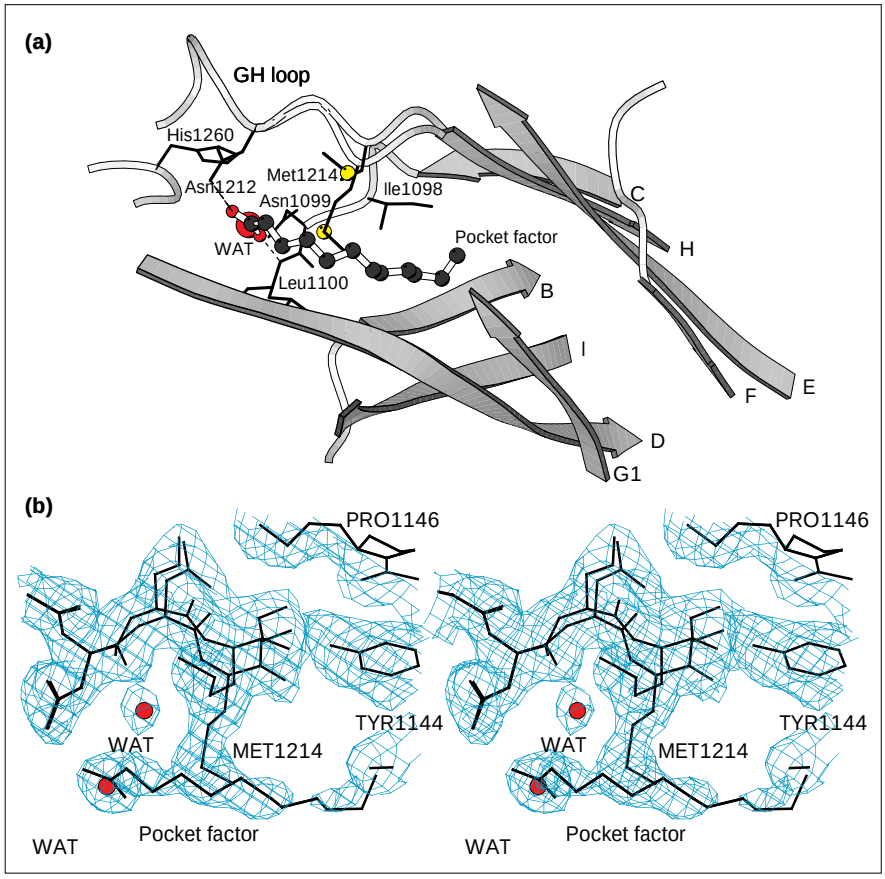

The hydrophobic pocket in VP1. (a) Diagrammatic view of the binding pocket in VP1 showing the eight β strands which make up the core of VP1. The floor of the canyon, where the cellular receptor ICAM-1 binds, lies at the top of the picture. Residues which have an atom lying within 4 Å of the pocket factor are shown with black bonds. The putative fatty acid representing the pocket factor is shown in ball-and-stick representation. Sulfur atoms are shown in yellow, carbon atoms in black, oxygen atoms in red and a water molecule is depicted as a large red sphere. The pocket factor as modeled makes two 2.8 Å hydrogen bonds shown with dashed lines. The GH loop, leading into strand H, contains the residues which adopt alternate conformations depending on the occupancy of the hydrophobic pocket. (This figure was created using MOLSCRIPT [64].) (b) Stereo view showing the electron density as calculated using data set II with a D_{min} of 2.15 Å, contoured at 3.0σ. The figure shows the portion of VP1 associated with the binding pocket, which has been modeled in two alternate conformations; water molecules are shown as red spheres.

hydrophobic pocket and is anchored by two hydrogen bonds (Fig. 1). The sidechains that lie within 4 Å of the pocket factor are indicated in Figure 1a and all lie at the solvent accessible end of the pocket. The electron density is weaker further from the head group of the modeled fatty acid, which could indicate that the pocket is occupied by fatty acids of variable length or could be because the aliphatic tail is more flexible, as there are no anchoring hydrogen bonds and no close van der Waals contacts.

The electron density from data set II has been interpreted as the superposition of two structures for the GH loop and strand H (residues 1210 to 1218) (Fig. 1b). Strand H lies across the top of the hydrophobic pocket close to the surface of the viral capsid forming the floor of the canyon. One conformation of the strand corresponds to the open form of the pocket, with the strand protruding and lifting the canyon floor. In the other conformation, the pocket is 'closed', resembling the native structure observed in HRV14 and the closely related HRV3 [21], with Met1214 (1221 in HRV14) in an extended conformation across the pocket factor binding site. In the closed conformation, a water molecule was modeled to take the position that the head group of the pocket factor occupied in the open form. The presence of the water molecule was inferred from the height of the density in this position and from the presence of a solvent molecule in the same position in HRV16–antiviral compound complexes, where the compound binds further into the hydrophobic end of the pocket (ATH, IM, DC Pevear and MGR, unpublished results).

The electron density for the pocket factor is discontinuous in the high resolution structure with a break between the strong electron density of the head group and the central portion and also a break towards the end of the tail of the pocket factor. There is a spherical shell of radius 3 Å, where the density approaches zero height, around each of the two alternative sulfur positions for Met1214. This is most likely a truncation effect due to the incompleteness of the data and would explain the two breaks of density in the pocket factor. Alternatively, the density interpreted as pocket factor, assumed to be a fatty acid, could be a solvent molecule plus a moiety the shape of a short aliphatic hydrocarbon. However, it would seem more likely that the pocket factor is a frequently occurring cellular product such as a fatty acid.

Figure 2

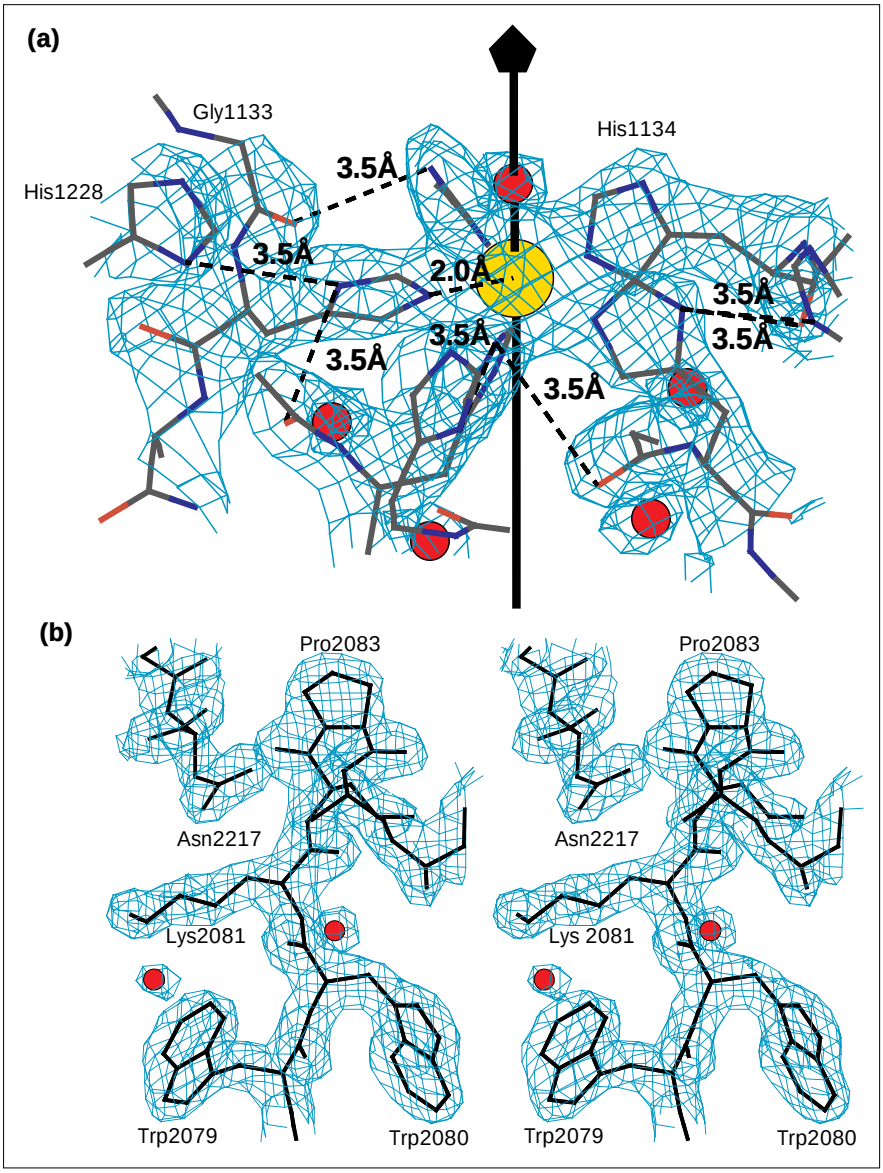

Regions of interesting electron density. (a) Electron density contoured at 3σ, from a map calculated using $F_{obsII}exp(i\alpha_{backII})$ showing the ion site at the top of the icosahedral fivefold axis. Distances between atoms are represented by dashed lines. The cation is shown as a large yellow sphere, nitrogen atoms are blue, oxygen atoms red, carbon atoms gray and water molecules are shown as large red spheres. The view, chosen for clarity, does not encompass one of the five water molecules observed below the ion. (b) Stereo view electron density contoured at 3σ from a map calculated using $F_{obsII}exp(i\alpha_{backII})$, showing the *cis* proline in VP2. Water molecules are shown in red.

Ion-binding site

There is high electron density near the exterior of the virus on the icosahedral fivefold axis at a distance of 152 Å from the center of the virion. This was interpreted as a Ca^{2+} ion liganded by the NE2 atoms of five symmetry-related histidines and a putative water molecule on the fivefold axis, towards the external side of the virus (Fig. 2a). The coordination distances of the NE2 atoms to the ion are 2.0 Å. Chemical considerations suggest that there could be a seventh oxygen ligand lying below the ion away from the fivefold symmetry axis. A water molecule performing this function would only occupy one of the five possible symmetry sites around each icosahedral symmetry axis, resulting in electron density too weak to be observed. The intensity of the ion electron-density peak is slightly stronger than that of the most intense sulfur peaks in the averaged electron-density maps. Therefore, if the ion is a Ca^{2+} or Zn^{2+}, the site is not fully occupied. The height of the electron density for the histidines is weaker than most of the protein electron density, suggesting that these residues are not well ordered. This could be because the ion site is not completely occupied or because the coordination does not obey the noncrystallographic symmetry.

There is a second group of five symmetry-related histidines (His1228) which may be interacting with the liganding histidines (His1134) (Fig. 2a). However, in the refined structure, the distance of 3.5 Å between the nitrogens (which

should act as donor and acceptor) is too great for a hydrogen bond. A similar long distance occurs between the donor nitrogen of His1134 and the carbonyl oxygen of residue 1136 on a symmetry-related polypeptide.

Calcium has been implicated previously in the uncoating process of a number of icosahedral viruses [22–24]. In HRV14, the equivalent site is most probably occupied by a Ca^{2+} ion [25]. In HRV16, the crystallization conditions include 20 mM Ca^{2+}, suggesting that the metal ion site on the fivefold axis is also occupied by a Ca^{2+} ion. However, no nitrogen atom has been observed as a ligand to a Ca^{2+} ion in a protein structure before, although pyridine bases have been observed as Ca^{2+} ligands in nucleotide complexes [26] with a nitrogen to Ca^{2+} distance of 2.7 Å. The refined liganding distance between the nitrogen and Ca^{2+} ions of 2.0 Å is rather short; a distance closer to 2.5–2.6 Å would be more typical. When there are six or more ligands, as in HRV16, the expected ligand distance would be longer rather than shorter. Shifts of the histidine ligands above and below the plane of the Ca^{2+} ion might allow a more appropriate distance. The site of the ion on a symmetry axis constrains the refinement to find the averaged position of the ligands, but it is possible that the liganding residues may lack fivefold symmetry.

On the other hand, histidine residues are quite frequently found to ligand Zn^{2+} ions, with a typical nitrogen–zinc distance of 2.2 Å in protein crystal structures. A study of Zn^{2+} ion complexes from the Cambridge Structural Database [27] reports that a coordination number of 5 or 6 is most common for a nitrogen ligand, and also reports structures with five nitrogen ligands and one or two oxygens. Zn^{2+} has also been implicated in the rhinovirus life cycle [26,28,29], with evidence that Zn^{2+} can be effective as a cold remedy [30–32]. It is, therefore, possible that Zn^{2+} may have been carried through the HRV16 purification process from the HeLa cells in which the virus was grown.

VP2

The N terminus of VP2 (residues 2001–2009) is not visible in HRV16 or most other picornaviruses. There is some weak, uninterpreted electron density on the icosahedral threefold axis near where the three symmetry-related N termini of VP2 come together. The structure based on data set II confirmed the presence of a *cis* proline at residue 2083 in the loop between strands C and D (Fig. 2b). Residues 2159–2163 in the so-called puff region of VP2, which corresponds to the neutralizing immunogenic site NIm II in HRV14, is badly defined with weak density for the mainchain atoms and no density for sidechain atoms. The two C-terminal residues 2260 and 2261 (not modeled by Oliveira *et al.*) could be clearly recognized. The amino acid type for residues 2024, 2026 and 2071 had been wrongly assigned in the original structure determination [3]. There is now good agreement between the published sequence [33] and the electron density for these residues (Thr2024, Gln2026 and Trp2071).

VP3

VP3 was the best defined protein in the original structure determination. Using data set II, an additional *cis* peptide bond has now been identified at Pro3093 in the loop between strands C and D, similar to the *cis* peptide in VP2. The electron density for residue 3218 in VP3 was inconsistent with the histidine assigned in the published sequence [33]. The electron density suggested that the residue could be an aspartate, which is a conserved residue in this position in all the picornaviruses except for hepatitis A and bovine enterovirus. The identity of this residue in HRV16 was confirmed as an aspartate on re-examination of the sequencing gels.

VP4

VP4 is less well defined than the other protein chains, which is reflected in the high temperature factors along most of its length. However, the electron density was visible in maps calculated using coefficients $F_{obs}\exp(i\alpha_{back})$ and maps calculated using coefficients $(F_{obs}-F_{calc})\exp(i\alpha_{calc})$, where the residues in question were omitted from the structure-factor calculation using coefficients $(F_{calc})\exp(i\alpha_{calc})$. There is relatively strong electron density just below the N-terminal β cylinder formed by VP3 in a position close to that observed for the N terminus of VP4 in poliovirus and coxsackievirus B3. This has been interpreted as the myristate head group and the N-terminal residues of VP4 (Fig. 3a). Two β strands (4001–4007 and 4023–4029) were recognized, which, together with the N-terminal strands from four symmetry-related molecules, form a ten-stranded, antiparallel, twisted β cylinder around the base of the fivefold axis (Fig. 3b). The N-terminal helices of VP1 pack around the outside of this β cylinder.

There is a network of hydrogen bonds close to the head of the myristate including a hydrogen bond linking the carbonyl oxygen of the myristate, to the hydroxyl group of Tyr1006 in the N-terminal amphipathic helix of the neighboring VP1 (Fig. 3c). While the head group and the first five carbon atoms of the myristate are well defined, there is weak or no electron density for the rest of the aliphatic chain. However, there are two pentagonal slabs of density centered on the fivefold axis with arms rather like a starfish, which suggest that the tail of the fatty acids come together to form a twisted barrel that runs inwards towards the virion center, as has been suggested for foot-and-mouth disease virus type C [34]. The residues which face inwards from the two N-terminal strands of VP4 (Gly4001, Ala4002, Val4004, Phe4027 and Leu4029) are hydrophobic in this portion of the ten-stranded β barrel, providing a good environment for the aliphatic portion of the myristate. The sidechains become more hydrophilic

Figure 3

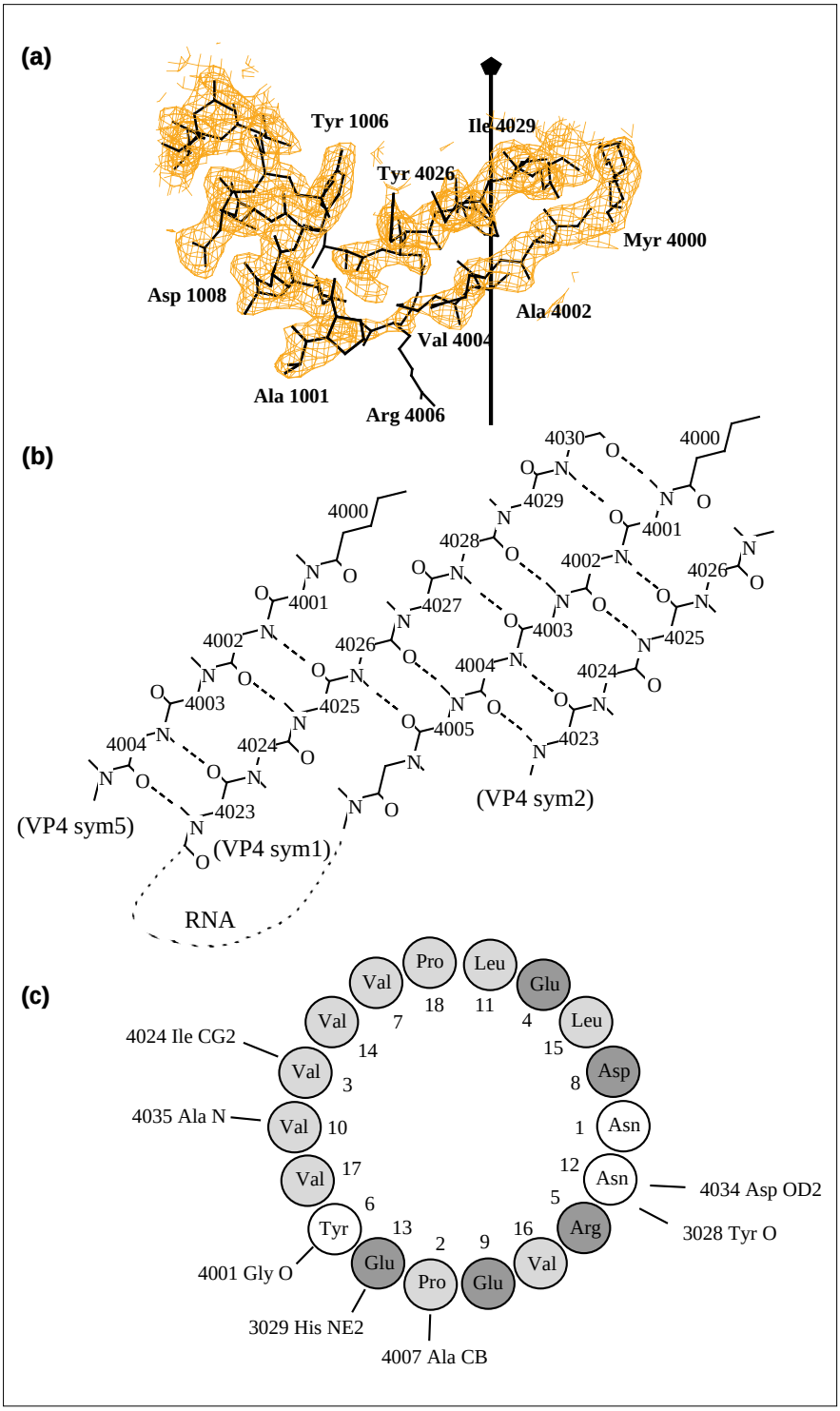

Structure around the fivefold axis. (a) Electron density around the icosahedral fivefold axis. The protein model is shown as bonds. The electron density was calculated using coefficients $F_{obsII}\exp(i\alpha_{backII})$ and contoured at 2σ for residues at the N termini of VP4 (4000–4030) and VP1 (1001–1012). (b) The hydrogen-bonding network in the β barrel formed by the symmetry-related N termini of VP4. Hydrogen bonds are indicated by dashed lines. The N terminus of the model is shown in the center (sym1), with its symmetry-related contacts on each side (sym2 and sym5). The dotted line shows the disordered part of one VP4 polypeptide associated with the viral RNA. (c) The N-terminal residues of VP1 form an amphipathic helix; the first 18 residues of HRV16 are shown as a helical wheel. The interactions between the N-terminal portion of VP1, which was observed as an α helix in the crystal structure, and the surrounding residues are indicated around the wheel with bars. Hydrophobic residues are indicated by light grey shading and hydrophilic residues are shown in dark grey.

closer to the center of the virion where they are in closer proximity to the RNA. However, the electron density becomes more featureless as VP4 penetrates into the RNA, with residues 4008 to 4022 being invisible.

VP4 was only modeled up to residue 4044, although VP4 actually has 68 residues. However, there is more or less continuous, but lower, density that is in essentially the same position as the mainchain residues 4045–4068 of

Table 2

Data collection and refinement statistics of HRV16.

Stage	Data set I*	Data set II†
Data collection‡		
Crystal-to-film distance (mm)	170	240
D_{min} (Å)	2.8	1.9
Number of crystals (No. images)	81 (225)	17 (89)
Number of reflections	1332 460	3442 752
Number of unique reflections	645 656	1452 910
Rejection criterion ($I > n\sigma(I)$)	3	1
R_{merge} (%)	11.1	9.7
Completeness ($\infty - D_{min}$)	63.1	44.5
Refinement§		
Data range (Å)	8.0–2.9	6.0–2.15
$F > n\sigma(F)$ where n =	3.0	3.0
Number of reflections in work set	564 008	1115 369
Number of reflections in test set	62 757	123 880
Number of cycles of Powell minimization	170	180
Final statistics		
R factor (%) (R_{free})	22.9 (23.3)	23.0 (23.3)
Protein model		
atoms	6349	6383
residues	805	797
Solvent (waters)	311	541
Non-protein atoms		
pocket factor	14	14
ion	1	1
Rms deviations from ideality for bonds (Å)	0.008	0.010
Rms deviations from ideality for angles (°)	1.40	1.50
Average B factors		
All protein atoms (Å^2)	10.7	17.5
(mainchain / sidechain)	(9.1 / 12.4)	(16.4 / 18.6)
Solvent molecules	23.9	30.8
Pocket moiety	27.3	23.7
VP1	11.6	19.3
VP2	8.5	14.7
VP3	7.3	14.1
VP4	47.0	50.8

*Images were collected using Kodak X-ray film at CHESS [3]. The oscillation angle was 0.3°; data were processed according to Rossmann [52] and Rossmann *et al.* [53]. †Images were collected using Fuji image plates at beamline F1, CHESS and scanned using 100 μm raster step size with a Fuji BAS2000 scanner. The oscillation angle was 0.25°; data were processed with the HKL package [54]. ‡The data were all collected at a temperature of 4°C and using X-rays with a wavelength of 0.91 Å. Exposure times for the image plates ranged from 8 to 20 s. §Crystallographic refinement performed using X-PLOR [60], with Engh–Huber [62] parameter sets.

VP4 in HRV14. There is little evidence for the position of sidechains, although a slab of density is in the same position as the sidechain of Phe4052 in HRV14. This density was consistently one of the highest peaks in $(F_{obs}–F_{calc})\exp(i\alpha_{calc})$ electron-density maps. The C terminus of VP4 is, therefore, in the vicinity of the N terminus of VP2, as would be anticipated by the final maturation cleavage of VP0 into VP2 and VP4 [4].

Analysis of temperature factors

The quality of the electron density is unusually good in places where the temperature factor is rather high (> 50 Å^2). A possible explanation is that the phasing can be rather accurate in the presence of high noncrystallographic symmetry. The temperature factors for the two refined native models show similar trends (Table 2), with areas of well defined secondary structure having the lower temperature factors while higher temperature factors are associated with residues in exposed loops (Fig. 4). VP3 and VP2 are more ordered than VP1; the temperature factors are most extreme in the case of VP4. VP4 lies within the viral capsid and presumably interacts with RNA along most of its length. As the single strand of RNA is not icosahedrally ordered for the most part, the conformation of VP4 is affected both by its interactions with the other viral proteins and its non-icosahedral interactions with the RNA. The temperature factors are lowest at the radius where the protein atom concentration is highest (Fig. 4b).

Figure 4

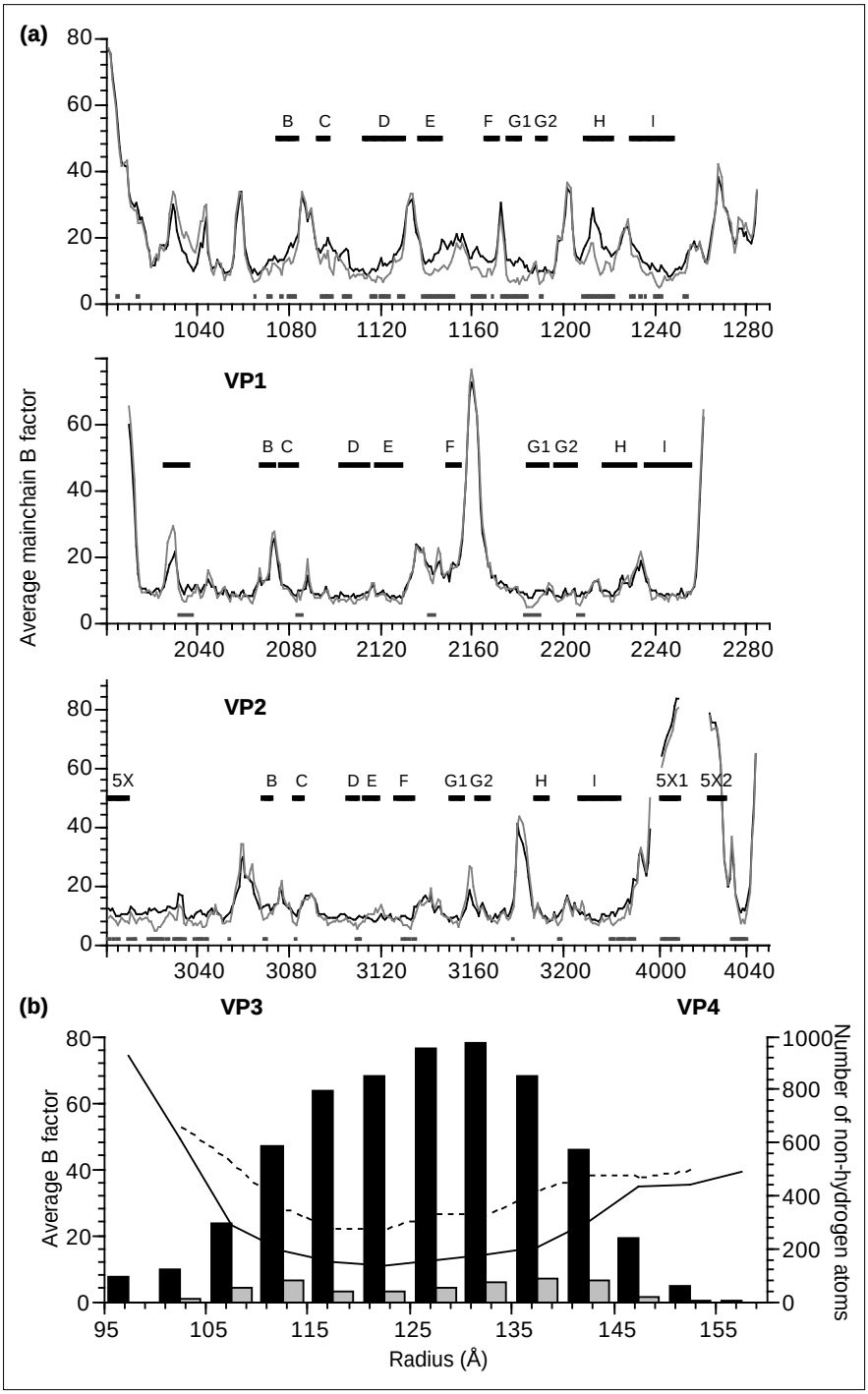

Analysis of temperature factors. **(a)** Average mainchain isotropic B factors of viral proteins VP1–VP4 in the HRV16 model. The B factors corresponding to data set II are shown in black lines, and those of HRV16 complexed with the antiviral compound WIN61209 are shown in gray lines for comparison. Places where the B factors differ by greater than one standard deviation are indicated below the plots in gray bars. The β strands in the viral proteins are indicated by black bars above the plots, with those forming barrels with symmetry-related copies at the fivefold axis marked '5X'. **(b)** Frequency distribution of protein atoms (black bars) and solvent atoms (gray bars) compared with the distribution of mean temperature factors for protein atoms (solid line) and solvent atoms (dashed line).

Three structures for HRV16–drug complexes have also been determined and refined (ATH, IM, DC Pevear and MGR, unpublished results). The temperature factors for the native structure and the virus–drug complex structures were compared and found to be similar for the most part. Figure 4a shows the residues where the difference in the average mainchain temperature factors for the native structure and for the HRV16–drug complexes is greater than one standard deviation. The larger differences are concentrated around the hydrophobic pocket in VP1 with all eight β strands from VP1 having lower temperature factors in the presence of an antiviral compound and,

Figure 5

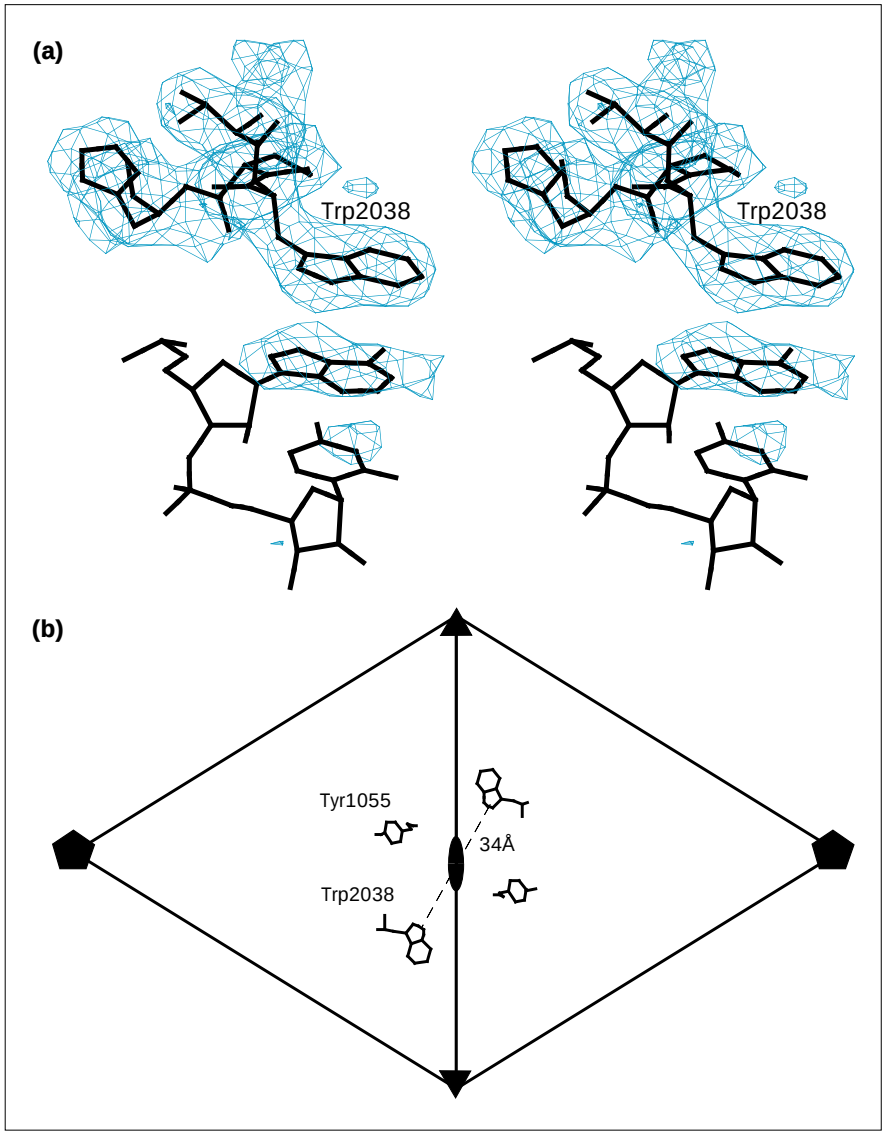

Ordered RNA structure. **(a)** Electron density in an averaged map calculated using coefficients $F_{obs}exp(i\alpha_{avl})$ and data with a D_{min} of 2.9 Å, contoured at 3.0σ. A model has been positioned in the electron density for two RNA bases stacking against the conserved residue Trp2038. **(b)** Diagram of the position of the residues against which stacking is observed, projected down the icosahedral twofold axis between two pentamers. For clarity, the sidechains are enlarged twofold relative to the size of the icosahedral asymmetric unit. The center of mass of the sidechains of Tyr1055 and Trp2038 are projected to their correct positions. The distance between twofold-related tryptophans is 34 Å (dashed line).

therefore, having less conformational flexibility than they do in the native structure. Similarly, the ion-binding site in two loops of VP1 becomes more occupied and the residues holding the ion in place become more ordered when the virus is complexed with an antiviral compound. This observation is consistent with the apparent increase in occupancy of the ion in the presence of the Winthrop (WIN) antiviral compounds (ATH, IM, DC Pevear and MGR, unpublished results). The differences in temperature factors between the native and complexed structures at the N terminus of VP3 were surprising. However, as residues 3014–3043 lie below the β barrel of VP1 the increase in order in this area in the presence of antiviral compounds is presumably propagated through interactions between VP3 and VP1.

Solvent molecules

The solvent molecules that have been included were identified in noncrystallographic symmetry averaged electron-density maps and, therefore, are icosahedrally ordered. Figure 4b shows an analysis of both temperature factors and the number of protein and solvent atoms as a function of the radius of the virus particle. There is a bimodal distribution of solvent molecules, with peaks on the outer and inner surfaces of the viral protein shell. There are fewer water molecules within the hydrophobic core of the viral capsid, but the temperature factors are lower in this region, where the water molecules have a greater number of potential hydrogen-bonding partners. The population of solvent molecules is greatest at distances of 135–140 Å from the center of the particle. There is another, slightly

lower peak at 110–115 Å on the inside of the capsid where the viral protein is assumed to be interacting with the RNA. It is probable that a number of electron-density peaks are due to other ions which have been packaged along with the RNA to neutralize its charge. Some peaks could also be phosphate ions, which would also make favorable interactions with charged groups on the interior of the capsid. Studies on poliovirus suggest that a single virion encapsidates about 4900 K^+ ions, 900 Na^+ ions, 110 Mg^{2+} ions and a few molecules of spermidine and putrescine [35]. In correspondence with the decrease in the order of the protein in the interior of the particle, the average temperature factor of the solvent molecules also increases. However, these molecules have been kept in the model because they consistently appeared in symmetry-averaged electron-density maps at a level where the protein density was well defined (3σ) and also appeared in difference maps when they were omitted from the model.

RNA structure

The averaged electron-density maps calculated using each data set show electron-density features within the capsid which cannot be assigned to viral protein (Fig. 5a). These features are strongest in the electron-density maps calculated using data set I, where the low resolution data are most complete. This density can be modeled as icosahedrally ordered RNA bases within the viral capsid. The strongest density is a flattened shape which lies at a distance of 4.0 Å from, and parallel to, the sidechain of Trp2038; a purine fits this density better than a pyrimidine. Another piece of flattened electron density is observed further into the interior of the particle, which is consistent with the size and shape of a pyrimidine. There is a separation of 3.5 Å between the planes of these two bases, consistent with them being two consecutive ribonucleotides. Similar electron density has been observed stacking against this residue in HRV14 [36], poliovirus [16,37] and coxsackievirus B3 [12]. Trp2038 is conserved throughout the picornaviruses and lies between the pseudo-threefold axis, where VP1, VP2 and VP3 come into contact, and the icosahedral twofold axis. Trp2038 is also on the edge of the trefoil depression, observed in the poliovirus empty capsid, which was proposed to bind RNA [38]. Another pair of bases can be tentatively identified stacking against residue Tyr1055. These bases also lie between the pseudo-threefold axis and the icosahedral twofold axis. Again, the density closest to the tyrosine corresponds well to the size of a purine base at a distance of 4 Å from the plane of the tyrosine. The second base lies with its plane 3.5 Å further towards the center of the viral particle. Residues 2038 and 1055 are situated at opposite ends of the interpentamer interface about the same distance from the twofold axis (Fig. 5b). The tryptophan residues in two adjacent pentamers are 34 Å apart, a distance corresponding to the length of one complete turn in a helical strand of RNA. The inner surface of the protein coat is slightly concave between these two residues.

Table 3

Site-directed mutagenesis of Trp2038.

Virus	Codon of residue 2038	Yield (PFU ml^{-1})*
Wild type	TGG	1.8×10^7
Trp2038→Phe	TTT	2.3×10^6
Trp2038→His	CAT	100
Trp2038→Val	GTG	100
Trp2038→Gly	GGT	10

*HeLa cells (7.5×10^6) were incubated with 2 μg of transcripts from mutant cDNA in 200 μg ml^{-1} DEAE dextran for 60 min at 23°C. Monolayers were washed with 10 ml phosphate buffered saline, then overlaid with 2.5 ml medium. After incubation at 35°C for 2 days, the cells were scraped free in the spent medium, the cell suspension was freeze-thawed three times, the cell debris was pelleted and the supernatant was collected and titrated.

Effect of substitutions at Trp2038 on viability of HRV16

Four different single mutations were introduced at Trp2038 by site-directed mutagenesis. After mutant transcripts were transfected into HeLa cells, virus yield was determined after 48 h incubation at 35°C (Table 3). Trp2038→Phe is the only viable mutant, with about an eightfold lower titer than compared to wild type. Mutants with histidine, valine and glycine substitutions produced no infectivity; the very low titer observed with these substitutions was probably due to revertants.

Discussion

The hydrophobic binding pocket

HRV14, a major group rhinovirus, was the first rhinovirus structure to be determined. The structure contained no pocket factor, although pocket factors were subsequently observed in all poliovirus [16,37,39], coxsackievirus B3 [12] and bovine enterovirus [40] structure determinations. The uncoating of bovine enterovirus can be inhibited by fatty acids. In addition, HRV1A, a minor receptor group rhinovirus, was found to contain a small pocket factor [11]. These observations were correlated with the ability of WIN compounds to inhibit attachment to the cellular receptor. On binding to HRV14, WIN compounds cause the conformation of the pocket to change from closed to open, thereby also changing the conformation of the floor of the canyon. WIN compounds are known to inhibit attachment in major group rhinoviruses, such as HRV14 and HRV16, but not in minor group rhinoviruses, such as HRV1A. In HRV1A, it was shown that displacement of the pocket factor by a WIN compound did not substantially alter the floor of the canyon. Hence, it was a considerable surprise [3] to observe a pocket factor in HRV16. This observation suggested that there is a dynamic equilibrium between the binding of a pocket factor or WIN compound and the binding of receptor [3,41,42]. The function of the

Figure 6

A schematic diagram representing VP1 of HRV16, showing the binding site of the pocket factor (shown in ball-and-stick representation) and the WIN antiviral compounds (shown in pale blue). A cation on the fivefold axis is shown in yellow. The N termini of VP1, VP3 and VP4 also interact around the fivefold axis. One copy of each of VP1 and the N termini of VP3 and VP4 are shown as blue, red and green ribbon diagrams, respectively. The myristylated N terminus of VP4 is labelled (MYR). (The diagram was created using MOLSCRIPT [64].)

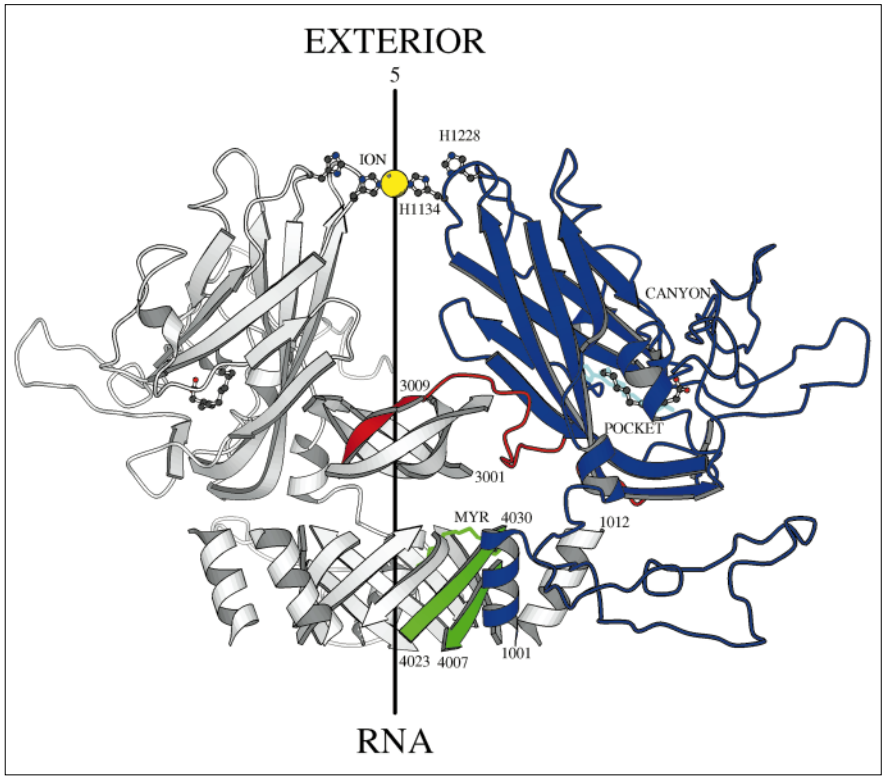

pocket factor is, therefore, thought to regulate the capsid stability prior to cell entry when the virus has to disassemble [3,16,18,42].

The 2.15 Å electron density-map of HRV16 shows both an open and a closed conformation of the pocket simultaneously. The partial substitution observed in this case supports the idea that HRV14 might bind a pocket factor weakly, but under the crystallization conditions (and long-term dialysis) it has dissociated. The binding affinity of the pocket factor, the stability of the virus and the affinity to the receptor all need to be carefully balanced in a viable virus.

The fivefold axis

The icosahedral fivefold axis has been suggested as a port of exit for the RNA during infection [43,44]. It has also been noted [12] that the shape of the channel along the fivefold axis in picornaviruses and the positioning of an ion at the 'top' of the axis is very similar to the shape of the fivefold channel in ϕX174 [23], where the fivefold axis is known to be the port of exit of the DNA. The fivefold axis has also been proposed to be the port of exit for RNA in the nodaviruses [45] and, more recently, the tetraviruses [46], where a pentameric bundle of helices is observed lying just below the particle surface. An alternative proposition for the uncoating of picornaviruses is the separation of the protomeric building blocks [38], reminiscent of the effect of removing Ca^{2+} from tomato bushy stunt virus [47].

In HRV16, the fivefold axis is capped with an ion liganded by histidine residues (Fig. 6). The ion is surrounded by symmetry-related copies of VP1, which are held together through the liganding of the ion and by association with the N terminus of VP3. The second constriction on the fivefold axis occurs where five copies of VP3 come together around the fivefold axis, forming a parallel β cylinder. Below VP3, two strands from each of five symmetry-related copies of VP4 form a twisted, antiparallel β cylinder, with the myristate at the N terminus forming a plug below the β barrel of VP3. The amphipathic helix at the N terminus of VP1 (Figs 3c and 6) packs against the outside of the ten-stranded β barrel of VP4. The internal diameter of the helical bundle is greater than 22 Å, similar to the comparable helical bundle observed in *Nudaurelia* ω *capensis* virus [46], and is sufficient to accommodate single-stranded RNA once VP4 is externalized.

It is known that, as a first stage in viral infection, VP4 is lost from the viral particle [48,49]. This can be induced ÿby acidic conditions or by incubation with the receptor, ICAM-1. The loss of VP4 is accompanied by the externalization of the N terminus of VP1, which was predicted

to be an amphipathic helix [18]. VP4, with its myristate forming a hydrophobic plug, is well positioned to leave the particle along a channel up the fivefold symmetry axis. The hydrogen bond observed in HRV16 between the N-terminal residue of VP4 and the N terminus of the VP1 helix could induce the externalization of the amphipathic helix along with the exit of VP4. It is notable that residues 14–63 of VP1 have no regular secondary structure, which is an energetic advantage in the externalization of the N terminus of VP1.

The hydrophobic constriction close to the inside of the particle is due to residues 3002–3010, which become more rigid in the presence of antiviral compounds, as indicated by the comparison of temperature factors. Similarly, the ion-binding site becomes more occupied and the residues holding the ion in place become more ordered when the virus is complexed with an antiviral compound. The presence of an antiviral compound also prevents uncoating, from which we can infer that the flexibility observed in the native state is important for uncoating to proceed. Residues at the N terminus of VP3 and in VP1 around the ion-binding site also become disordered upon acidification of rhinovirus, a condition which induces uncoating [44].

The reduction in flexibility in the VP1 β barrel and the N terminus of VP3 on binding antiviral compounds is consistent with mechanisms of infectivity that require separation of protomeric building blocks in the vicinity of VP1, including the mechanism of Hogle [38]. However, VP4 and the N terminus of VP1 do not seem as conveniently located to exit at the pseudo- threefold axes.

RNA

In the crystal structure of cowpea chlorotic mottle virus, Trp47 interacts with RNA [24] and has been shown to be necessary for the assembly of full, RNA containing particles (X Zhang, M Young and RJ Kuhn, personal communication). Binding of RNA to pentamers and full capsids has been observed in poliovirus [50] where the RNA induces conformational changes that might initiate the assembly process. Trp2038, which is associated with putative RNA density in rhino-, coxsackie- and polioviruses, is present in all picornaviruses and is well placed to bind a strand of RNA across the interface between two pentamers, which might catalyze the assembly process.

The tyrosine residue observed to interact with RNA in VP1 lies on the part of VP1 which is disordered in empty particles of HRV16 (WW Farrar, MAO, MGR, unpublished results). In poliovirus, the corresponding residue would be a histidine and is two residues away from the first ordered residue observed in the poliovirus empty capsid structure [38]. It is possible that interaction between the RNA and this residue is partly responsible for the disorder→order transition between empty and full virions.

Biological implications

Rhinoviruses belong to the picornavirus family and are small, icosahedral, non-enveloped particles containing one positive RNA strand. Rhino- and enteroviruses can be inhibited by a variety of capsid-binding compounds that inhibit uncoating and, in some cases, attachment. Some of these compounds have now been through clinical trials, including tests where HRV16 was used as a pathogen. Hence, an analysis of the HRV16 structure and its properties was initiated and reported on some time ago [3]. In this paper, we report a higher resolution structure which shows a number of new details relevant to viral cell entry, RNA packaging and properties of the hydrophobic pocket in VP1 that binds the antiviral compounds.

The refined structure shows previously unobserved portions of VP1 and VP4. VP4, which is myristylated, and the N terminus of VP1 interact at the fivefold axis. Differences are observed in the flexibility of the protein along this axis in the presence of compounds which prevent uncoating of the virus. Together, this information suggests that the loss of VP4 and externalization of the N terminus of VP1, which are the preliminary steps in virion uncoating, may occur at the fivefold axis. Release of an ion that binds on the fivefold axis near the outside of the virion, accompanied by increased flexibility around the channel around the fivefold axis, may allow VP4 to leave the particle. When VP4 leaves the particle, VP1 may become externalized in the same process through hydrogen-bonding contacts with VP4. The amphipathic helices observed at the N termini of five symmetry-related copies of VP1 are well placed to form a pore through the membrane for the eventual release of RNA along this axis.

Icosahedrally ordered RNA was observed to bind at a tryptophan and a phenylalanine site close to the interface between adjacent pentamers. Non-conservative mutations of the tryptophan results in non-viable virus. The tryptophan may play a role in the assembly of icosahedral particles from pentameric intermediates.

Materials and methods

Virus preparation and crystal growth

HRV16 was prepared and crystallized as previously described [3]. The virus crystallized in space group $P2_12_12$, with cell dimensions a = 362.56, b = 347.11, c = 334.90 Å. The crystallographic twofold axis coincides with an icosahedral twofold symmetry axis, allowing for 30-fold noncrystallographic symmetry averaging.

Site-directed mutagenesis of HRV16

The original stock of HRV16 was a gift from EC Dick, University of Wisconsin, Madison. HRV16 was passaged in mycoplasma free H1-HeLa cells [33]. HRV16 full-length duplex complementary DNA clone was constructed as previously described [2]. This cDNA clone (pR16.11) produces infectious transcripts (WL and RRR, unpublished results).

Site-directed mutations were introduced into VP2 using a mutagenesis cassette vector and synthetic oligodeoxyribonucleotide primers. The

Figure 7

Construction of the cassette vector p1AB for site-directed mutagenesis. Numbers in parentheses identify the nucleotide for restriction enzyme cleavage.

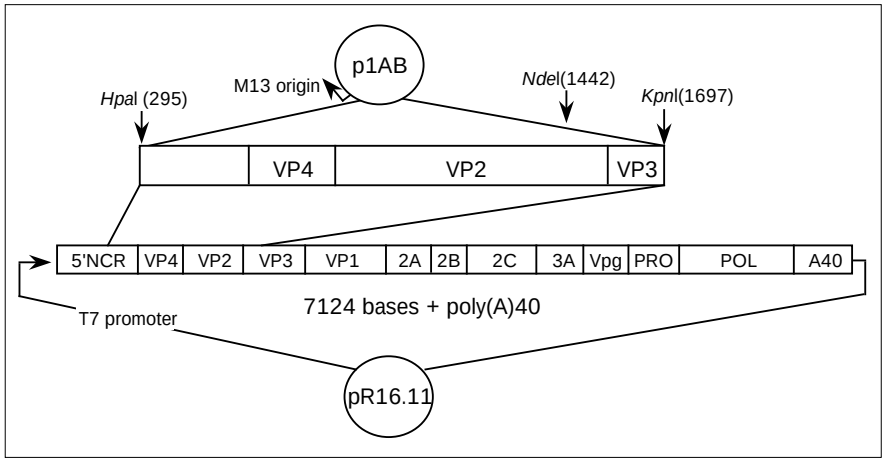

cassette vector (p1AB; Fig. 7) was constructed by inserting the *Hpa*I–*Kpn*I (295–1697 nucleotide sequence) fragment of pR16.11 plasmid into the pMJ3 vector.

By using the method of Kunkel [51], vector p1AB yielded M13-packaged uracil-enriched single-stranded DNA with the opposite sense of virion RNA; mutagenesis was performed as described by Kunkel [51]. The cassette regions of selected mutant plasmids were completely sequenced to confirm that no non-specific mutation crept in during *in vitro* DNA analysis.

For generating a full-length clone with a site-directed mutation in VP2, the *Hpa*I–*Nde*I fragment (295–1442 nucleotide sequence) of the pR16.11 plasmid was replaced with a homologous fragment from the mutated p1AB plasmid.

Plasmid pR16.11 DNA, or its mutant derivative, was linearized by *Sac*I restriction enzyme *in vitro* and transcribed using T7 RNA polymerase [2]. The product was electrophoresed in a 0.8% agarose gel along with a known amount of virion RNA. The gel was stained with ethidium bromide to estimate the amount of full-length transcripts.

Infectivity of transcripts was assayed in 100 mm monolayers of H1-HeLa cells (7.5 million cells). The monolayers were transfected with 2 μg RNA as described [2]. Transfected monolayers were incubated at 35°C for 2 days. Cells were scraped free in the spent medium, the cell suspension was freeze-thawed three times, cell debris was pelleted and supernatant was collected and titered. Infectivity of whole virus was assayed in 60 mm monolayers of H1-HeLa cells (2.5 million cells), as described [2].

Data collection and processing

Both native data sets were collected at the Cornell High Energy Synchrotron Source (CHESS). Data set I (extending to 2.9 Å resolution) was collected on film [3], processed and refined (Table 2) using the Purdue University suite of programs [52,53]. The more recent data set II (extending to 2.1 Å resolution) was collected on imaging plates with a crystal-to-film distance short enough to record more of the high resolution reflections than had been possible for data set I. Data set II was processed and refined using the HKL package [54] (Table 2).

Particle position and orientation

The particle orientation was re-determined by fitting a standard icosahedron to the peaks in a rotation function computed using data between 4 and 3.5 Å resolution. The single translational parameter and the single rotational parameter were then examined in a rigid-body refinement procedure using the original structure [3]. The position of the particle was checked once more using an iterative averaging process which minimized the scatter of electron density between non-crystallographically related subunits [55], but no further shift in particle position was observed.

Phase refinement and electron-density calculations

Parallel versions of programs developed at Purdue University were used for electron-density calculations and modification [56]. The first cycle of electron-density averaging always used unit weights for all reflections to avoid biasing towards the starting model. New structure factors (F_{back}) and phases (α_{back}) were calculated in each cycle by back-transforming the averaged electron-density map. The next cycle began with the calculation of an electron-density map using coefficients $F_{obs}\exp(i\alpha_{back})$. After two or three cycles, a geometric combination of Sim weights and Rayment weights [57] were used. For data set II, which was rather incomplete, calculated structure factors were included in the electron-density map after three cycles of averaging, with weights equal to the average in the resolution shell. Iterative cycles of electron-density averaging and phase combination were performed until there was no further improvement in the correlation between the observed structure factors and the back-transformed structure factors (approximately ten cycles). A spherical shell with an outer radius of 165 Å and inner radius of 80 Å was used as a mask for averaging.

Model building and map interpretation

Model building was performed using the program O [58]. The program PROCHECK [59] was used to monitor the geometry of the model at various stages in refinement. Parts of the model with poor geometry were rebuilt into averaged electron-density maps. Both iteratively averaged maps with coefficients $F_{obs}\exp(i\alpha_{back})$ and difference maps with coefficients $(F_{obs}-F_{calc})\exp(i\alpha_{calc})$ were used for identifying other inconsistencies in the models. Structure factors were computed using X-PLOR [60].

Crystallographic refinement

The atomic coordinates for the two models were refined by conjugate-gradient minimization using X-PLOR [60]. Strict noncrystallographic symmetry was imposed throughout the refinement procedures, thus reducing the number of parameters to those that describe the structure of one noncrystallographic asymmetric unit. The X-ray crystallographic energy term minimized was:

$$W_a/N_a\Sigma_h w_h\,[|F_{obs}(h)|-k|F_{calc}(h)|]^2$$

where W_a is an overall weight between the X-ray crystallographic term and the empirical energy term, N_a is a normalization factor, h are the

miller indices of the structure-factor amplitudes, w_h are the weights for individual reflections and k is a scale factor. The W_a used was equal to half the weight obtained by running a short molecular dynamics calculation and comparing the normal of the gradient of the empirical energy terms to the X-ray energy term [61].

A free R factor was monitored using 10% of the data. This was generally within 0.1% of the working R factor because of the high degree of correlation between the data due to the imposition of noncrystallographic symmetry. The test data were purposely kept fairly large to demonstrate the effect of high noncrystallographic symmetry on the free R factor relative to the working R factor. The Engh–Huber parameters were used to describe the protein in the refinement [62]. A model for the putative fatty acid in the hydrophobic binding pocket was based on the Engh–Huber parameters for glutamate (the atoms around the head group) and CHARMm parameters for the aliphatic carbons [63]. The model for a myristate moiety was similar to the fatty-acid model. A patch was written to covalently link the fatty acid to the N terminus of VP4 based on a peptide linkage. The cation was constrained to the icosahedral fivefold symmetry axis during refinement. Weak force constants were used to restrain the bond distance between the ligands and the ion, to allow the crystallographic data to drive the refinement. The final step was restrained refinement of individual isotropic temperature factors.

The Oliveira *et al.* model [3] was rebuilt using an averaged electron-density map calculated at 3.5 Å resolution. This model, including bulk solvent, was refined in X-PLOR by conjugate-gradient minimization using data from 30 to 3.5 Å resolution. The refined structure was used to calculate phases, α_{calc}, directly to 2.15 Å resolution. The phases were combined with the observed amplitudes of data set I (F_{obs}) to calculate a new electron-density map to 2.9 Å resolution. This 2.9 Å resolution electron-density map was used to initiate 30 cycles of electron-density averaging using the mask described above. The back-transformed phases were used to compute a difference map with coefficients $(F_{obsI}–F_{obsII})\exp(i\alpha_{back})$. This showed that there was substantially less pocket factor in the virions of crystals used in the collection of data set II. Therefore, the data sets were not combined. The calculated phases were combined with the observed amplitudes from data set II for calculation of an electron-density map to 2.15 Å resolution.

The new averaged electron-density maps were used to rebuild the models. A Ca^{2+} ion was placed on the fivefold axis, some ordered water molecules were included and a fatty acid was built to represent the pocket factor in the model based on data set I. The model corresponding to data set I was refined using data from 10 Å to 2.9 Å resolution for 160 steps of Powell minimization [60], with model inspection and rebuilding after every 40 steps.

A difference map with coefficients $(F_{obsII}–F_{calcII})\exp(i\alpha_{calcII})$ was calculated after 40 cycles of conjugate-gradient minimization of a model with no pocket factor corresponding to data set II using data from 8.0 Å to 2.15 Å. Positive electron density confirmed the presence of the pocket factor. At this point, two alternatives were modeled for residues 1210–1218 in VP1 and some rebuilding was performed. In a map calculated using coefficients $F_{obsII}\exp(i\alpha_{back})$, the averaged electron density for Met1214 had two well defined peaks for the alternate sulfur positions. The heights of these electron-density peaks were roughly equal, implying approximately 50% occupancy of the pocket. The occupancy for each of the alternate conformations was, therefore, set to 0.5. The model was then refined for a further 140 steps of conjugate-gradient minimization, with model inspection and rebuilding after every 40 steps. In these calculations, all the data were used for map calculations, but only the data between 6.0 and 2.1 Å were used for refinement.

Five residues lie within generously allowed regions of the Ramachandran plot: Thr3195, Asn2113, Trp3027, Asp2057 and Asn2030. Of these residues, Thr3195 and Asn2113 form a hydrogen bond at the interface between pentamers. Residues 3027 and 2057 both lie on the inner face of the particle and make contact with two other symmetry-related protomers within a single pentamer. Residue 2030 also lies on the inner face of the particle and is positioned above a stretch of VP4 which is too poorly ordered to be interpretable. The apparently unusual geometry in this position is probably due to interactions with VP4.

Water molecules were considered real if they had a height above 1.5σ of the electron density in both the averaged map (with coefficients $F_{obsI}\exp(i\alpha_{back})$) and a difference map (with coefficients $(F_{obsI}–F_{calc})\exp(i\alpha_{calc})$) and also had reasonable coordination with the protein or with other water molecules. Each water molecule was refined with full occupancy, but using an independent temperature factor. However, the water molecule that was modeled into the closed conformation of the pocket associated with data set II was assumed to have an occupancy of 0.5.

Accession numbers

The coordinates and structure-factor amplitudes were submitted to the Brookhaven Protein Data Bank prior to publication of this paper (deposition number BNL 3759).

Acknowledgements

We thank Dan Marinescu, Robert Lynch and Marius Cornea-Hasegan for their development of molecular replacement programs on parallel computers. We are also grateful to Cheryl Towell and Sharon Wilder for help in the preparation of the manuscript. The work was supported by National Institutes of Health grant (AI 11219) to MGR and by a Lucille P Markey award for the support of structural biology at Purdue University.

References

1. Rueckert, R.R. (1996). Picornaviridae: the viruses and their replication. In *Virology*. (Fields, B.N., Knipe, D.M. & Howley, P.M., eds), pp. 609–654, Lippincott-Raven Press, New York.
2. Lee, W., Monroe, S.S. & Rueckert, R.R. (1993). Role of maturation cleavage in infectivity of picornaviruses: activation of an infectosome. *J. Virol.* **67**, 2110–2122.
3. Oliveira, M.A., *et al.*, & Rossmann, M.G. (1993). The structure of human rhinovirus 16. *Structure* **1**, 51–68.
4. Rossmann, M.G., *et al.*, & Vriend, G. (1985). Structure of a human common cold virus and functional relationship to other picornaviruses. *Nature* **317**, 145–153.
5. Abraham, G. & Colonno, R.J. (1984). Many rhinovirus serotypes share the same cellular receptor. *J. Virol.* **51**, 340–345.
6. Greve, J.M., *et al.*, & McClelland, A. (1989). The major human rhinovirus receptor is ICAM-1. *Cell* **56**, 839–847.
7. Staunton, D.E., Merluzzi, V.J., Rothlein, R., Barton, R., Marling, S.D. & Springer, T.A. (1989). A cell adhesion molecule, ICAM-1, is the major surface receptor for rhinoviruses. *Cell* **56**, 849–853.
8. Olson, N.H., *et al.*, & Rossmann, M.G. (1993). Structure of a human rhinovirus complexed with its receptor molecule. *Proc. Natl. Acad. Sci. USA* **90**, 507–511.
9. Smith, T.J., *et al.*, & Otto, M.J. (1986). The site of attachment in human rhinovirus 14 for antiviral agents that inhibit uncoating. *Science* **233**, 1286–1293.
10. Grant, R.A., Hiremath, C.N., Filman, D.J., Syed, R., Andries, K. & Hogle, J.M. (1994). Structures of poliovirus complexes with anti-viral drugs: implications for viral stability and drug design. *Curr. Biol.* **4**, 784–797.
11. Kim, K.H., *et al.*, & Pevear, D.C. (1993). A comparison of the anti-rhinoviral drug binding pocket in HRV14 and HRV1A. *J. Mol. Biol.* **230**, 206–225.
12. Muckelbauer, J.K., *et al.*, & Rossmann. M.G. (1995). The structure of coxsackievirus B3 at 3.5 Å resolution. *Structure* **3**, 653–667.
13. McSharry, J.J., Caliguiri, L.A. & Eggers, H.J. (1979). Inhibition of uncoating of poliovirus by arildone, a new antiviral drug. *Virology* **97**, 307–315.
14. Diana, G.D., *et al.*, & Pancic, F. (1977). Antiviral activity of some β-diketones. 1. Aryl alkyl diketones. *In vitro* activity against both RNA and DNA viruses. *J. Med. Chem.* **20**, 750–756.
15. Pevear, D.C., *et al.*, & Dutko, F.J. (1989). Conformational change in the floor of the human rhinovirus canyon blocks adsorption to HeLa cell receptors. *J. Virol.* **63**, 2002–2007.
16. Filman, D.J., Syed, R., Chow, M., Macadam, A.J., Minor, P.D. & Hogle, J.M. (1989). Structural factors that control conformational transitions and serotype specificity in type 3 poliovirus. *EMBO J.* **8**, 1567–1579.

17. Hoover-Litty, H. & Greve, J.M. (1993). Formation of rhinovirus-soluble ICAM-1 complexes and conformational changes in the virion. *J. Virol.* **67**, 390–397.
18. Fricks, C.E. & Hogle, J.M. (1990). Cell-induced conformational change in poliovirus: externalization of the amino terminus of VP1 is responsible for liposome binding. *J. Virol.* **64**, 1934–1945.
19. Casanovas, J.M. & Springer, T.A. (1994). Pathway of rhinovirus disruption by soluble intercellular adhesion molecule 1 (ICAM-1): an intermediate in which ICAM-1 is bound and RNA is released. *J. Virol.* **68**, 5882–5889.
20. Moscufo, N., Yafal, A.G., Rogove, A., Hogle, J. & Chow, M. (1993). A mutation in VP4 defines a new step in the late stages of cell entry by poliovirus. *J. Virol.* **67**, 5075–5078.
21. Zhao, R., *et al.*, & Rossmann, M.G. (1996). Human rhinovirus 3 at 3.0 Å resolution. *Structure* **4**, 1205–1220.
22. Harrison, S.C., Olson, A.J., Schutt, C.E., Winkler, F.K. & Bricogne, G. (1978). Tomato bushy stunt virus at 2.9 Å resolution. *Nature* **276**, 368–373.
23. McKenna, R., *et al.*, & Incardona, N.L. (1992). Atomic structure of single-stranded DNA bacteriophage ϕX174 and its functional implications. *Nature* **355**, 137–143.
24. Speir, J.A., Munshi, S., Wang, G., Baker, T.S. & Johnson, J.E. (1995). Structures of the native and swollen forms of cowpea chlorotic mottle virus determined by X-ray crystallography and cryo electron microscopy. *Structure* **3**, 63–78.
25. Zhao, R., Hadfield, A.T., Kremer, M.J. & Rossmann, M.G. (1997). Cations in human rhinoviruses. *Virology*, **227**, 13–23.
26. Brown, E.A. & Bugg, C.E. (1980). Calcium-binding to nucleotides: structure of a hydrated calcium salt of inosine 5′-monophosphate. *Acta Cryst. B* **36**, 2597–2604.
27. Bock, C.W., Katz, A.K. & Glusker, J.P. (1995). Hydration of zinc ions: a comparison with magnesium and beryllium ions. *J. Am. Chem. Soc.* **117**, 3754–3765.
28. Korant, B.D., Kauer, J.C. & Butterworth, B.E. (1974). Zinc ions inhibit replication of rhinoviruses. *Nature* **248**, 588–590.
29. Korant, B.D. & Butterworth, B.E. (1976). Inhibition by zinc of rhinovirus protein cleavage: interaction of zinc with capsid polypeptides. *J. Virol.* **18**, 298–306.
30. Eby, G.A., Davis, D.R. & Halcomb, W.W. (1984). Reduction in duration of common colds by zinc gluconate lozenges in a double-blind study. *Antimicrob. Agents Chemother.* **25**, 20–24.
31. Godfrey, J.C. (1988). Zinc for the common cold. *Antimicrob. Agents Chemother.* **32**, 605–606.
32. Godfrey, J.C., Conant-Sloane, B., Smith, D.S., Turco, J.H., Mercer, N. & Godfrey, N.J. (1992). Zinc gluconate and the common cold: a controlled clinical study. *J. Int. Med. Res.* **20**, 234–246.
33. Lee, W., Wang, W. & Rueckert, R.R. (1994). Complete sequence of the RNA genome of human rhinovirus 16, a clinically useful common cold virus belonging to the ICAM-1 receptor group. *Virus Genes* **9**, 177–181.
34. Lea, S., *et al.*, & Mateu, M.G (1994). The structure and antigenicity of a type C foot-and-mouth disease virus. *Structure* **2**, 123–139.
35. Koch, F. & Koch, G. (1985). *The Molecular Biology of Poliovirus*. Springer-Verlag, New York.
36. Arnold, E. & Rossmann, M.G. (1990). Analysis of the structure of a common cold virus, human rhinovirus 14, refined at a resolution of 3.0 Å. *J. Mol. Biol.* **211**, 763–801.
37. Flore, O., Fricks, C.E., Filman, D.J. & Hogle, J.M. (1990). Conformational changes in poliovirus assembly and cell entry. *Semin. Virol.* **1**, 429–438.
38. Basavappa, R., Syed, R., Flore, O., Icenogle, J.P., Filman, D.J. & Hogle, J.M. (1994). Role and mechanism of the maturation cleavage of VP0 in poliovirus assembly: structure of the empty capsid assembly intermediate at 2.9 Å resolution. *Protein Sci.* **3**, 1651–1669.
39. Yeates, T.O., *et al.*, & Hogle, J.M. (1991). Three-dimensional structure of a mouse-adapted type 2/type 1 poliovirus chimera. *EMBO J.* **10**, 2331–2341.
40. Smyth, M., Tate, J., Hoey, E., Lyons, C., Martin, S. & Stuart, D. (1995). Implications for viral uncoating from the structure of bovine enterovirus. *Nat. Struct. Biol.* **2**, 224–231.
41. Hadfield, A.T., *et al.*, & Rossmann, M.G. (1995). Structural studies on human rhinovirus 14 drug-resistant compensation mutants. *J. Mol. Biol.* **253**, 61–73.
42. Rossmann, M.G. (1994). Viral cell recognition and entry. *Protein Sci.* **3**, 1712–1725.
43. Mosser, A.G., Sgro, J.-Y. & Rueckert, R.R. (1995). WIN51711-resistant mutants of poliovirus type 3: capsid residues important in uncoating functions. *Acta Cryst. D* **51**, 490–495.
44. Giranda, V.L., *et al.*, & Rueckert, R.R. (1992). Acid-induced structural changes in human rhinovirus 14: possible role in uncoating. *Proc. Natl. Acad. Sci. USA* **89**, 10213–10217.
45. Cheng, R.H., Reddy, V.S., Olson, N.H., Fisher, A.J., Baker, T.S. & Johnson, J.E. (1994). Functional implications of quasi-equivalence in a *T* = 3 icosahedral animal virus established by cryo-electron microscopy and X-ray crystallography. *Structure* **2**, 271–282.
46. Munshi, S., *et al.*, & Johnson, J. (1996). The 2.8 Å structure of a T = 4 animal virus and its implications for membrane translocation of RNA. *J. Mol. Biol.* **261**, 1–10.
47. Robinson, I.K. & Harrison, S.C. (1982). Structure of the expanded state of tomato bushy stunt virus. *Nature* **297**, 563–568.
48. Lonberg-Holm, K. & Korant, B.D. (1972). Early interaction of rhinoviruses with host cells. *J. Virol.* **9**, 29–40.
49. Everaert, L., Vrijsen, R. & Boeyé, A. (1989). Eclipse products of poliovirus after cold-synchronized infection of HeLa cells. *Virology* **171**, 76–82.
50. Nugent, C.I. & Kirkegaard, K. (1995). RNA binding properties of poliovirus subviral particles. *J. Virol.* **69**, 13–22.
51. Kunkel, T.A. (1987). Rapid and efficient site-specific mutagenesis without phenotypic selection. *Methods Enzymol.* **154**, 367–382.
52. Rossmann, M.G. (1979). Processing oscillation diffraction data for very large unit cells with an automatic convolution technique and profile fitting. *J. Appl. Cryst.* **12**, 225–238.
53. Rossmann, M.G., Leslie, A.G.W., Abdel-Meguid, S.S. & Tsukihara, T. (1979). Processing and post-refinement of oscillation camera data. *J. Appl. Cryst.* **12**, 570–581.
54. Otwinowski, Z. (1993). Oscillation data reduction program. In *Proceedings of the CCP4 Study Weekend: Data Collection and Processing*. (Sawyer, L., Isaacs, N. & Bailey, S., eds), pp. 59–62, SERC Daresbury Laboratory, Warrington, UK.
55. Muckelbauer, J.K., *et al.*, & Rossmann. M.G. (1995). Structure determination of coxsackievirus B3 to 3.5 Å resolution. *Acta Cryst. D* **51**, 871–887.
56. Cornea-Hasegan, M.A., *et al.*, & Rossmann. M.G. (1995). Phase refinement and extension by means of non–crystallographic symmetry averaging using parallel computers. *Acta Cryst. D* **51**, 749–759.
57. Arnold, E. & Rossmann, M.G. (1988). The use of molecular-replacement phases for the refinement of the human rhinovirus 14 structure. *Acta Cryst. A* **44**, 270–282.
58. Jones, T.A., Zou, J.-Y., Cowan, S.W. & Kjeldgaard, M. (1991). Improved methods for building protein models in electron-density maps and the location of errors in these models. *Acta Cryst. A* **47**, 110–119.
59. Laskowski, R.A., MacArthur, M.W., Moss, D.S. & Thornton, J.M. (1993). PROCHECK: a program to check the stereochemistry quality of protein structures. *J. Appl. Cryst.* **26**, 283–291.
60. Brünger, A.T. (1992). *X-PLOR, Version 3.1 Manual: A System for X-ray Crystallography and NMR*. Yale University Press, New Haven.
61. Weis, W.I., Brünger, A.T., Skehel, J.J. & Wiley, D.C. (1990). Refining influenza virus haemagglutinin. *J. Mol. Biol.* **212**, 737–761.
62. Engh, R.A. & Huber, R. (1991). Accurate bond and angle parameters for X-ray protein structure refinement. *Acta Cryst. A* **47**, 392–400.
63. Brooks, B.R., Bruccoleri, R.E., Olafson, B.D., States, D.J., Swaminathan, S. & Karplus, M. (1983). CHARMm: a program for macromolecular energy, minimization and dynamics calculations. *J. Comput. Chem.* **4**, 187–217.
64. Kraulis, P. (1991). MOLSCRIPT: a program to produce both detailed and schematic plots of protein structures. *J. Appl. Cryst.* **24**, 946–950.